

Synthetic Wavelength Holography: Snapshot Non-Line-of-Sight Imaging with High-Resolution and Wide Field of View

Florian Willomitzer^{1,*}, Prasanna V. Rangarajan², Fengqiang Li¹, Muralidhar M. Balaji², Marc P. Christensen², and Oliver Cossairt¹

¹Department of Electrical and Computer Engineering, Northwestern University, Evanston, IL 60208

²Department of Electrical and Computer Engineering, Southern Methodist University, Dallas, TX 75205

*Correspondence: florian.willomitzer@northwestern.edu

The presence of a scattering medium in the imaging path between an object and an observer is known to severely limit the visual acuity of the imaging system. We present an approach to circumvent the deleterious effects of scattering, by exploiting spectral correlations in scattered wavefronts. Our Synthetic Wavelength Holography (SWH) method is able to recover a holographic representation of hidden targets with high resolution over a wide field of view. The complete object field is recorded in a snapshot-fashion, by monitoring the scattered light return in a small probe area. This unique combination of attributes opens up a plethora of new Non-Line-of-Sight imaging applications ranging from medical imaging and forensics, to early-warning navigation systems and reconnaissance. Adapting the findings of this work to other wave phenomena will help unlock a wider gamut of applications beyond those envisioned in this paper.

Introduction

There are numerous instances of imaging within the physical sciences wherein an opaque barrier (such as a wall) or a scattering medium (such as fog or tissue) impedes direct view of the object. Over the years, many attempts [1–13] have been made to non-invasively recover images of objects obscured from direct view. These techniques are collectively referred to as 'Non Line-of-Sight Imaging' (NLoS) in our work. The problem is enjoying renewed attention due to emerging applications in autonomous navigation, planetary exploration, industrial inspection, and early-warning systems for first-responders [14–23].

Broadly speaking, current approaches to NLoS imaging circumvent the effect of scatter in one of two geometries: discrete scattering events distributed across multiple interfaces such as walls, and continuous scattering within a volume such as fog or tissue. Herein, we introduce a holographic approach - "Synthetic Wavelength Holography" (SWH) - that advances the state-of-the-art in NLoS imaging by exploiting spectral correlations in scattered light to see through any scattering geometry.

We make specific use of the observation that coherent light at two closely spaced wavelengths λ_1, λ_2 traversing near identical geometric paths in a scattering medium, preserves phase information at scales exceeding a 'Synthetic Wave-

length' (SWL) $\Lambda \gg \lambda_1, \lambda_2$ [24, 25]. We provide experimental evidence corroborating the above claim. Moreover, we establish that the optimal choice of the SWL scales with increasing scatter, and the synthetic phase computed at the distal end of the scattering medium encodes a holographic description of the obscured objects. The mathematical principles underlying the proposed imager concept expand the understanding of light transport in the presence of scatter.

A specific embodiment of the NLoS imaging problem is the task of looking around corners. We use this task to introduce the proposed approach and provide a basis for the comparative assessment with competing approaches. Existing schemes for imaging around corners attempt to recover the obscured scene by either exploiting the finite speed of light ("Time of Flight" *ToF* based techniques [16–19]) or spatial correlations in scattered light ("Memory Effect" *ME* based techniques [20, 25–29]).

ToF based NLoS Imaging techniques recover a surface representation of the hidden scene by probing the scene with a temporally modulated source, and recording the response using fast detectors. The process is repeated across multiple spatial locations (so-called 'virtual sources and detectors' - *VS* and *VD*) of an intermediary surface such as a wall or floor that is simultaneously visible to the obscured objects and the NLoS sensor unit. Recent work in the area [16–19] has demonstrated results with *cm*-scale lateral resolution over a $1m \times 1m \times 1m$ volume, and in select cases providing near real-time reconstructions. The approach, however, is limited by the need for raster-scanning large areas on the intermediary *VS/VD* surface whose dimensions are comparable to the obscured volume.

The second class of techniques for imaging around corners exploits spatial or angular correlations in scattered light [20, 25–29]. The images of obscured objects recovered using these techniques feature the highest lateral resolution ($< 100\mu m$ at $1m$ standoff), for the smallest probing area on the intermediary *VS/VD* surface ($< \text{few } cm$). The improved resolution, however, comes at the expense of a highly restricted angular *FoV* ($< 2^\circ$), as determined by the angular decorrelation of scattered light (Memory Effect [30, 31]). The *ME* does not only limit the *FoV*, but also (even more severe!) the maximal possible size of the measured object

Non-Line-of-Sight Imaging Capabilities of Synthetic Wavelength Holography

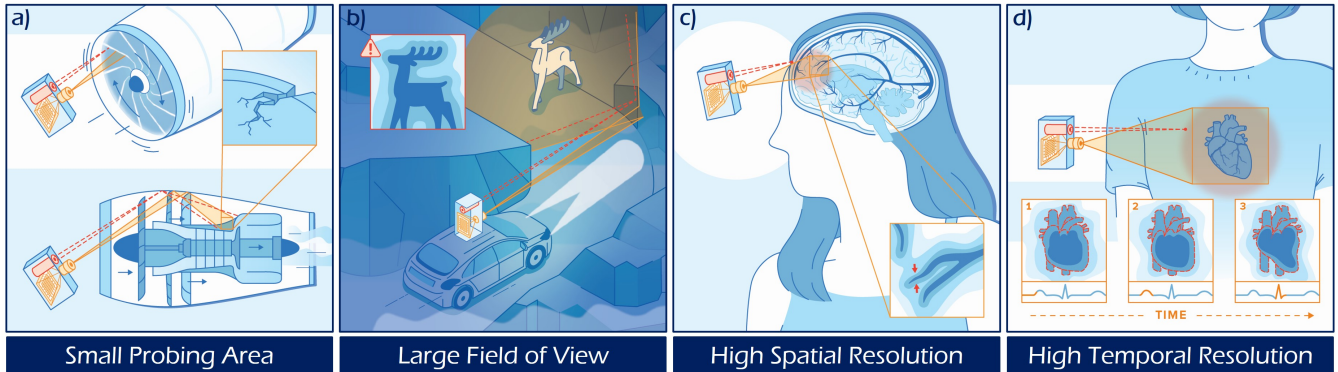


Fig. 1. Imaging objects obscured from direct view using 'Synthetic Wavelength Holography'(SWL). The approach combines four key attributes highlighted in the following NLoS application scenarios: In each example, a scattering surface or medium is used to indirectly illuminate, and intercept light scattered by the hidden objects. a) A small probing area allows to inspect defects in tightly confined spaces, e.g., in running aircraft engines. b) A large FoV allows to measure/detect hidden objects without previous knowledge of their position as, e.g., important when navigating in degraded visual environments. c) High spatial resolution allows for the measurement of small structures, such as non-invasive imaging of brain vessels through the skull. d) High temporal resolution allows to image objects in motion, e.g., to discern cardiac arrhythmia through the chest. The combination of these attributes in a single approach is unprecedented in the current state of the art.

84 which cannot be larger than the FoV. 120

85 The wide disparity in the FoV and resolution of cur- 121
 86 rent NLoS Imaging schemes greatly limits their utility. We 122
 87 demonstrate how to recover a truly holographic description 123
 88 of the obscured scene with a high spatial resolution, over a 124
 89 wide field of regard. Our SWH approach exploits *spectral* 125
 90 *correlations in scattered light* at optical wavelengths λ_1, λ_2 126
 91 to assemble a hologram of the obscured objects at the SWL 127
 92 $\Lambda = \frac{\lambda_1 \lambda_2}{|\lambda_1 - \lambda_2|}$. The approach combines a unique set of capabil- 128
 93 ities in providing a degree of versatility that is unmatched by 129
 94 competing NLoS approaches: 130

- 95 • **Small Probing Area** (see Fig. 1a): ToF based NLoS 131
 96 schemes use probing areas $\sim 1m \times 1m$. SWH provides 132
 97 the ability to image obscured objects in tightly con- 133
 98 fined spaces by simultaneously illuminating and ob- 134
 99 serving a small area ($58mm \times 58mm$ in our experi- 135
 100 ments). Potential applications include inline defect de- 136
 101 tection and inspection in heavy machinery such as run- 137
 102 ning turbines, and endoscopic imaging applications. 138
- 103 • **Large Field of View** (see Fig. 1b): ME-based ap- 139
 104 proaches produce highly restricted FOVs ($< 2^\circ$ for dry- 140
 105 wall), while SWH provides the ability to recover holo- 141
 106 grams of obscured objects over a hemispherical FoV 142
 107 that far exceeds the limited angular extent of the mem- 143
 108 ory effect. Potential applications include the design of 144
 109 early-warning systems in automotive sensing and plan- 145
 110 etary exploration. 146
- 111 • **High Spatial Resolution** (see Fig. 1c): ToF-based ap- 147
 112 proaches produce low spatial resolutions ($\sim cm$). SWH 148
 113 provides the ability to resolve small features on ob- 149
 114 scured objects (up to $< 1mm$ in our experiments) with- 150
 115 out requiring prior knowledge of the scattering geom- 151
 116 etry or attributes of the scattering medium such as the 152
 117 transmission matrix [32, 33]. Potential applications in- 153
 118 clude non-invasive imaging of blood vessels through 154
 119 tissue. 155

- **High Temporal Resolution** (see Fig. 1d): ToF-based 131
 approaches require point-wise raster-scanning, while 132
 SWH provides the ability to recover holograms of the 133
 obscured object in a snapshot fashion using conven- 134
 tional focal plane array (FPA) technology. This al- 135
 lows to resolve object motion such as sensing cardiac 136
 arrhythmia's through the chest, and remotely sensing 137
 surface motion of small planetary bodies [34]. 138

The mathematical principles underlying SWH are by no means restricted to the applications discussed above. The approach can be adapted to other NLoS imaging tasks including imaging through deep turbulence, fog and turbid waters, imaging through optically opaque barriers such as the skull, or face identification around corners. The idea of utilizing wavelength diversity to alleviate the effects of unwanted aberrations in the detection of electromagnetic signals has potential applications that go far beyond the original scope of NLoS imaging. We conclude this paper by discussing benefits of applying the SWH principle in a diverse set of application areas such as medical ultrasound, synchrotron X-ray diffraction imaging, and radio astronomy.

Synthetic Wavelength Holography (SWH)

Holographic approaches to imaging, including SWH, exploit the availability of a coherent source for illumination and interferometric sensing. Repeated scattering irreversibly randomizes the interference so that the speckle pattern recorded on the detector bears no resemblance to the macroscopic structure of the object.

However, a small change in the interrogation wavelength produces a largely identical speckle pattern with residual changes in phase that encode the macroscopic structure of the obscured object [24, 25]. We exploit this fact to probe the scattering medium at two closely spaced wavelengths λ_1 and λ_2 , and record the emerging speckle fields $E(\lambda_1)$ and $E(\lambda_2)$, as illustrated in Fig. 2a. Computational mixing of

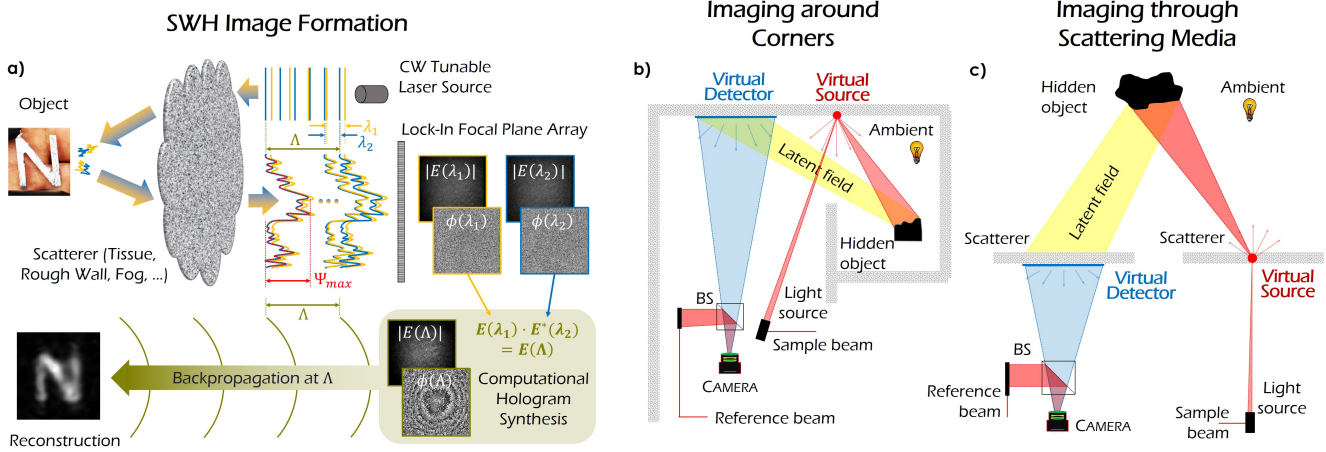


Fig. 2. Schematics of SWH for NLoS imaging around corners and NLoS imaging through scattering media. a) SWH image formation: A CW-tunable laser illuminates the scene at two slightly different wavelength λ_1 and λ_2 . Each field $E(\lambda_1)$, $E(\lambda_2)$ is subject to multiple scattering processes in or at the scatterer (which could be wall, tissue, fog,...) and the rough object surface. The introduced maximal pathlength variation Ψ_{max} leads to a complete randomization of $E(\lambda_1)$, $E(\lambda_2)$ when arriving at the detector. However, computational mixing of the speckled fields $E(\lambda_1) \cdot E^*(\lambda_2) = E(\Lambda)$, yields a complex-valued hologram of the object at a ‘Synthetic Wavelength’ (SWL) $\Lambda = \frac{\lambda_1 \cdot \lambda_2}{|\lambda_1 - \lambda_2|}$. The object is reconstructed by backpropagating $E(\Lambda)$ with the SWL Λ . b) and c) Schematic setups for NLoS imaging around corners (b) and NLoS imaging through scatterers (c) with the SWH principle: The sample beam illuminates a spot on the wall/scatterer (the ‘Virtual Source’ VS), which scatters light towards the obscured object. A small fraction of the light incident on the object is scattered back to the wall/scatterer where it hits the ‘Virtual Detector’ (VD). The VD is imaged by the camera, meaning that the synthetic hologram is captured at the VD surface.

155 the fields $E(\lambda_1) \cdot E^*(\lambda_2) = E(\Lambda)$, yields a complex-valued 188
 156 hologram of the object at the SWL $\Lambda = \frac{\lambda_1 \cdot \lambda_2}{|\lambda_1 - \lambda_2|}$ (see Fig. 2a). 189
 157 For closely spaced optical wavelength λ_1 and λ_2 , the SWL 190
 158 is orders of magnitude larger than λ_1, λ_2 so that the compu- 191
 159 tationally recovered field $E(\Lambda)$ is robust to the deleterious 192
 160 effects of scattering. An image of the hidden object can be 193
 161 retrieved by numerical backpropagation of $E(\Lambda)$ at the SWL 194
 162 Λ , as illustrated in Fig. 2a. 195

163 The strikingly simple and computationally inexpensive 196
 164 strategy described above can significantly improve the vi- 197
 165 sual acuity of imaging systems confounded by scatter. The 198
 166 computational immunity to scatter afforded by the existence 199
 167 of spectral correlations, relies only on the wave nature of 200
 168 light. As a consequence, the principles underlying SWH can 201
 169 be readily extended to other wave phenomena such as radio 202
 170 waves and acoustic waves (ultrasound). 203

171 Experimental Validation of SWH for Different 205 172 NLoS Imaging Techniques 206

173 ‘Looking around corners’. 208

174 We use the scene arrangement depicted in Figure 2b to eluci- 209
 175 date the SWH principle and demonstrate the ability to record 210
 176 holograms of objects beyond the line-of-sight. The portions 211
 177 of the wall designated VS and VD are used to indirectly il- 212
 178 luminate the hidden object, intercept the scattered latent field 213
 179 and relay it towards a focal plane array (FPA) that records the 214
 180 scattered field. Details of the image acquisition process and 215
 181 the imaging apparatus are provided in the methods section 216
 182 and the supplementary material. An image of the obscured 217
 183 object is recovered as explained above, i.e., by mixing the 218
 184 scattered optical fields $E(\lambda_1)$ and $E(\lambda_2)$ and playing back 219
 185 the assembled synthetic wavelength hologram $E(\Lambda)$ with the 220
 186 SWL Λ . The use of tunable lasers allows us to accommodate 221
 187 a variety of scattering scales by freely tuning the SWL over 222

a wide interval ranging from hundreds of μm to hundreds of m .

Figures 3a-e illustrate the phase of the computationally assembled synthetic wavelength hologram, for a specific set of SWLs. In each case, we are able to recover optical phase information, despite the pronounced scattering at the wall and object surface. The outcome of back-propagating the synthetic holograms is shown in Figs. 3f-j. The results confirm the ability to recover an image of a small object, character ‘N’ (dimensions $15mm \times 20mm$, see Fig. 3q) that is obscured from view. Furthermore, the *phase information* encapsulated in the synthetic hologram allows us to locate the hidden object within the obscured volume (illustrated in Fig. 5 and described later).

Figures 3f-j confirm that the resolution of the reconstruction improves with decreasing SWL Λ . This behavior is in agreement with results from classical holography. It implies that the synthetic wave, although a computational construct, has distinct characteristics that it shares with a physical wave at the respective wavelength Λ . The notion is corroborated in Fig. 3k-p wherein we attempt to localize a point-source obscured from view. It is observed that a diffraction limit may be ascribed to the computationally assembled synthetic hologram, in much the same manner as classical holography. The radius of the resulting ‘Synthetic Diffraction Disc’ is given by:

$$\delta x \approx \Lambda \frac{z}{D}, \quad (1)$$

where D is the diameter of the probing area at the VD, and z is the propagation distance to the object. The ratio $D/2z$ defines the numerical aperture of the computational NLoS-imager. In the present example, a lateral resolution limit of $\delta x = 800\mu m$ is reached for a SWL of $\Lambda = 280\mu m$. Details of the experiment are included in the methods section.

The expression for the resolving power of SWH disclosed

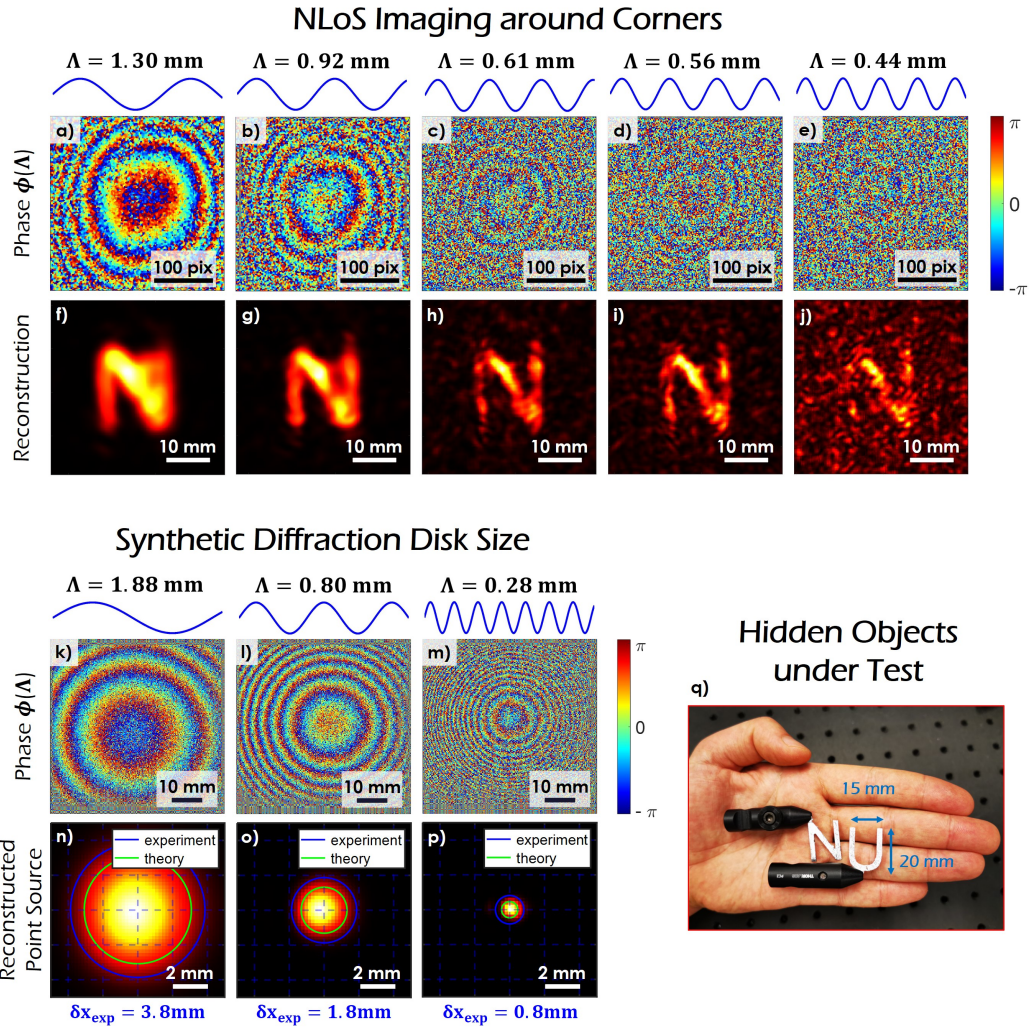


Fig. 3. Experimental results for imaging around corners with SWH. a)-j) Imaging the character 'N' ($\sim 15\text{mm} \times 20\text{mm}$) at five different SWLs. a)-e) The phase of the synthetic holograms at the VD surface. f)-j) Respective reconstructions. The resolution of the reconstructions increases with decreasing SWL. However, the speckle-artifacts increase due to the decorrelation of the two optical fields at λ_1 and λ_2 . k)-p) Reconstruction of an obscured point source for three different SWLs. k)-m) Phase of the synthetic holograms at the VD surface. n)-p) Reconstruction of the 'synthetic diffraction disc'. As in classical optics, the disc size varies linearly with the wavelength (in this case the SWL). The experimental value is close to the theoretical expectation. For p), the point source is reconstructed with sub-mm precision. q) Image of the targets used in the experiments of this paper: Two characters 'N' and 'U' with dimensions $\sim 15\text{mm} \times 20\text{mm}$ (plus black mountings).

in Eq. 1, suggests that the resolution may be indefinitely improved by reducing the SWL Λ . This however is not the case. For increasingly small values of Λ , the reconstructions exhibit speckle-like artifacts (see e.g. Figs 3f-j). The artifacts are attributed to a loss in the spectral correlation of the scattered fields observed at λ_1, λ_2 . The physical origins of this decorrelation are well documented in literature [31, 35–46]. The supplementary material includes a derivation for the specific case of 'looking around corners'.

'Looking through scatter' .

The notion of exploiting spectral correlations for NLoS imaging is by no means restricted to the 'looking around corners' problem. To highlight the versatility of the SWH approach, we recover holograms of objects embedded beneath a scattering medium, as illustrated in the schematic of Fig. 2c. In a first set of measurements, we image the small character 'U' (dimensions $15\text{mm} \times 20\text{mm}$, see Fig. 3q) through a 220-grit diffuser (Fig. 4a top). The holographic reconstructions

are displayed in Fig. 4b-e. As the SWL falls below $300\mu\text{m}$, we begin to notice 'synthetic speckle' artifacts in the reconstructed image, suggesting that wavelength separation has increased to the point that the captured optical holograms are uncorrelated for this specific scene.

In a second set of experiments, we swap the diffuser in the imaging path with a 4mm thick milky white plastic plate. Figure 4a illustrates the impact of pronounced multiple scattering on the visibility of a checkerboard that is viewed through the plastic plate and the 220 grit ground glass diffuser. It is clear from the results of Figs. 4f-i that we are able to reconstruct the character 'U' for SWLs $\Lambda \geq 360\mu\text{m}$. The results confirm the ability to recover image information at visibility levels that are far below the perceptual threshold, due in large part to scattering.

A comparison of the reconstruction results for the plastic plate and the diffuser reveals only a marginal change in the smallest achievable SWL, as we switch from thin scattering surfaces to thick scattering media. The implications of this

NLoS Imaging through Scatterers

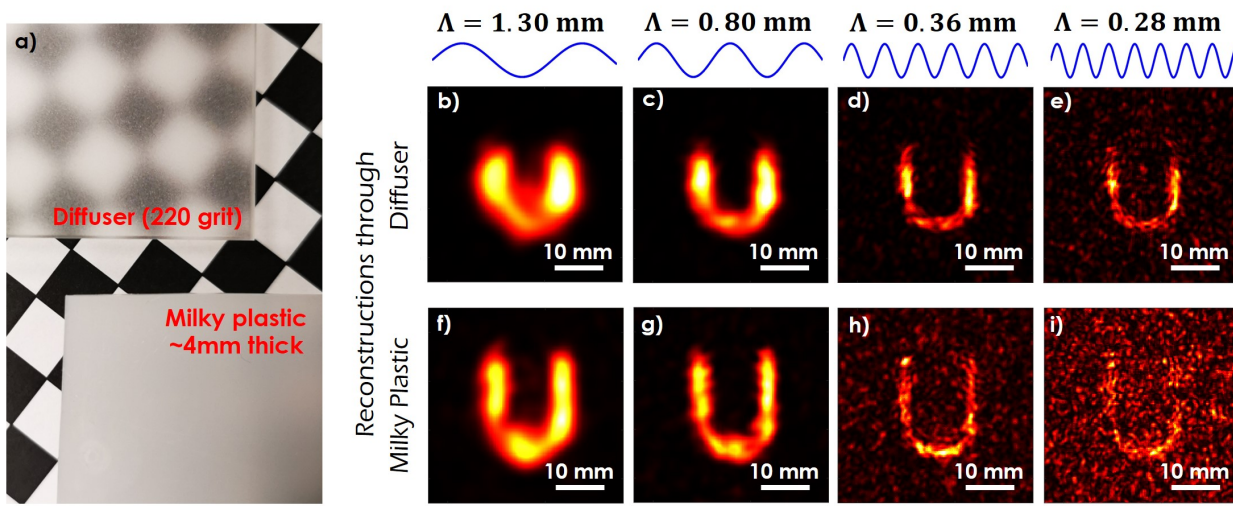


Fig. 4. Experimental results for imaging through scattering media with SWH. A schematic of the experimental setup is available in Fig. 2c. a) Scatterers obscuring the object: A 220 grit ground glass diffuser and a milky white plastic plate of $\sim 4\text{mm}$ thickness, both placed $\sim 1\text{cm}$ over a checker pattern to demonstrate the degradation in visibility. b)-e) Reconstructions of measurements taken through the ground glass diffuser. f)-i) Reconstructions of measurements taken through the milky plastic plate. The character can be reconstructed with impressive quality. The larger OPD in the plastic plate leads to greater decorrelation if the SWL is decreased.

258 observation are best understood by recognizing that the vis- 268
 259 ibility of ballistic light paths decays exponentially with the 269
 260 propagation distance through a scattering volume (in accor- 270
 261 dance with Beer's law [47]).

Synthetic Pulse Holography.

262 The principles underlying the proposed SWH concept can be 274
 263 extended to include multiple illumination wavelengths. The 275
 264 resulting spectral diversity is expected to yield an improve- 276
 265 ment in the longitudinal resolution, in much the same man- 277
 266 ner as Optical Coherence Tomography (OCT) [49–52] and 278

White-Light Interferometry (WLI) [53, 54]. However, unlike
 OCT and WLI, we do not need to match the power and path-
 lengths in the two interferometer arms.

271 To demonstrate the improvement in longitudinal resolution
 272 afforded by the use of multiple SWLs, we computa-
 273 tionally section a three-dimensional NLoS scene comprised
 of two previously introduced characters 'N' and 'U' (both
 $15\text{mm} \times 20\text{mm}$) that are offset in depth by $\Delta z \approx 33\text{mm}$. Us-
 ing a single SWL of $\Lambda = 800\mu\text{m}$ it is possible to separate the
 characters laterally, but with limited longitudinal resolution,
 as shown in Figs. 5b-e. Since we have access to the complex-

Synthetic Pulse Holography

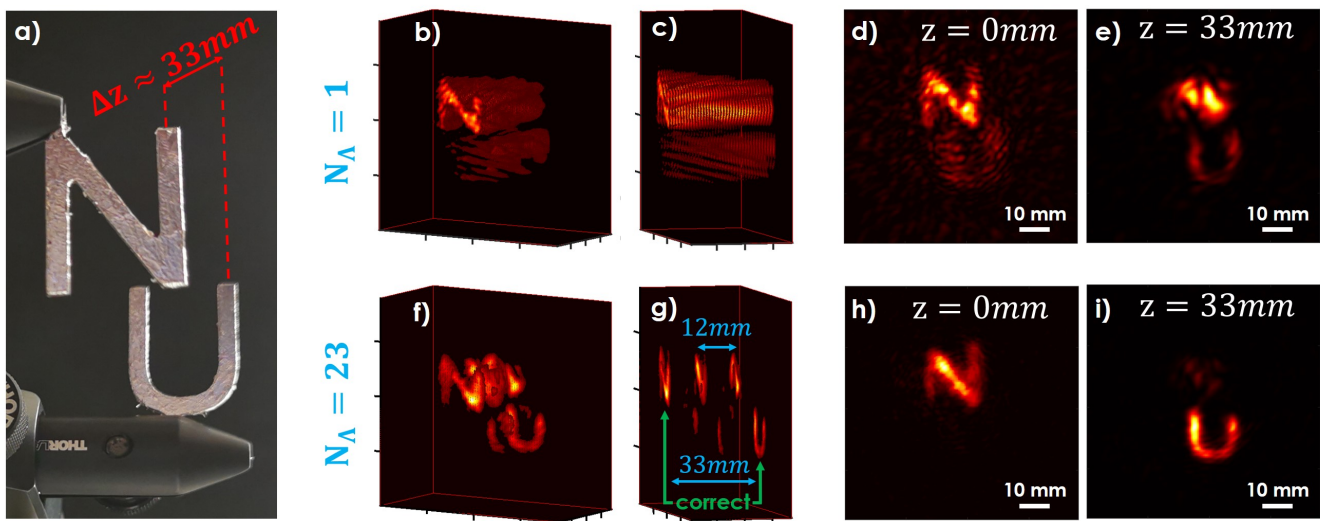


Fig. 5. Experimental Results for the generation of a 'synthetic pulse train' with SHW. a) Target, consisting of two characters with a longitudinal separation of 33mm . b)-e) Reconstruction of the characters, using only $N_\Lambda = 1$ SWL ($\Lambda = 0.8\text{mm}$). Due to the properties of holographic backpropagation, a separation of the characters in depth is not possible. f)-i) Reconstruction, calculated from coherent superposition of the backpropagated fields at $N_\Lambda = 23$ SWLs. Letters are separable. The pulse distance of the synthesized pulse train can be seen in (f) and (g).

valued field information at each synthetic wavelength, it is possible to improve the longitudinal resolution of SWH by coherently combining the synthetic fields recorded at a multitude of synthetic wavelengths ($N_\Lambda = 23$ in Fig. 5). The computational approach mimics scene interrogation by a periodic pulse train, and the replicas observed in the reconstructions of Fig. 5f and 5g are consistent with the periodicity of the computationally engineered pulse train (frequency offset of $25GHz$ corresponding to a depth ambiguity of $12mm$). An unambiguous measurement range in excess of $33mm$ requires a frequency increment of $\sim 1GHz$, which has been experimentally verified with our laser system as well. It is anticipated that locking the tunable laser source to a frequency ruler such as a frequency comb will further improve the longitudinal resolution, due in large part to the precise phase relationship between the individual comb teeth [55–57].

NLoS Wavefront Sensing.

The experiments in SWH described thus far have restricted attention to recovering objects obscured by scattering media. However, the principle underlying SWH, namely spectral correlations in scattered light, is rather general and has broader appeal. We demonstrate the ability to recover residual phase variations in the wavefronts emerging from a volumetric scattering sample. The data for this experiment were captured by the authors of [48] without the original intention to be used for our approach. Details of the experimental apparatus are available in Kadobianskyi et.al. [48]. The authors recorded speckle fields emerging from $720\mu m$ (Fig. 6a,b) and $1080\mu m$ (Fig. 6d,e) thick scattering samples with a scattering mean free path of $90\mu m$. In each case, the sample is interrogated by a quasi-monochromatic collimated beam at 801 equally spaced wavelength steps spanning the range $690nm$ to $940nm$. By computationally mixing speckle holograms recorded at adjacent wavelengths, we are able to identify a hologram at the SWL of $\Lambda = 2.1mm$. Results from the experiment are shown in Fig. 6. The phase of the synthetic

hologram exhibits a distinct spatial structure that is consistent with the observation of interference fringes due to inter-reflections between the laser aperture and a polarized beam splitter in the illumination path; according to the authors of [48]. It is worth emphasizing that the wavefront sensing approach described above, relies only on the scattered light paths as the ballistic paths are expected to be extinguished by factors of 10^{-8} and 10^{-12} in the $720\mu m$ and $1080\mu m$ sample respectively.

Discussion and Conclusion

The present work combines the expressive power of holography with spectral correlations in scattered light to tackle the challenging problem of NLoS imaging. Using only a small probing area ($58mm \times 58mm$ in our experiments), we are able to recover a high-resolution (up to $< 1mm$) holographic representation of obscured objects, over a hemispherical FoV. The technique is robust enough to accommodate different NLoS imaging scales (looking around corners to looking through fog) and scattering geometries (scattering at multiple interfaces to volumetric scatter).

The use of continuous wave sources at different wavelengths allowed us to bypass the need for ultrafast sources (picosecond pulses) and fast detectors (SPAD detectors, streak cameras), both of which are routinely employed in competing NLoS approaches. The use of full-field focal plane arrays additionally allowed us to bypass the need for raster scanning in ToF based NLoS schemes.

The SWH approach, however, is not without limitations, chief of which is the inability to recover phase information when the optical fields at the two wavelengths $E(\lambda_1)$ and $E(\lambda_2)$ are uncorrelated. It manifests as speckle-like artifacts in the reconstructed images at the SWL ('synthetic speckle'), such as those observed in Figs. 3j and 4i. The problem may be avoided by judicious selection of the interrogation wavelengths λ_1, λ_2 . It is observed that phase fluctuations ex-

Wavefront Sensing through Scatterers

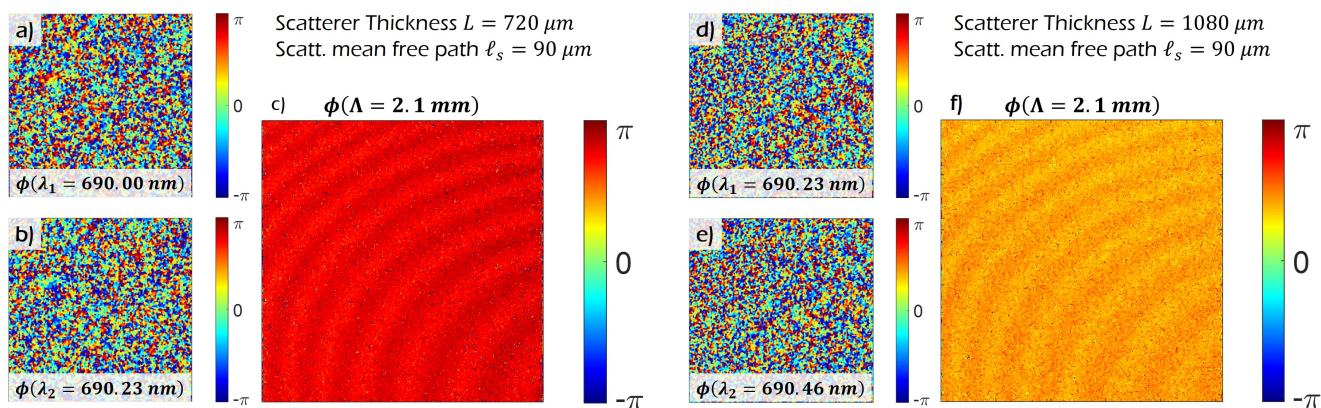


Fig. 6. Experimental Results for Wavefront sensing through scatterers with SWH. The data for this experiment were captured by the authors of [48] without the intention to be used for our approach. Nevertheless, our SHW reconstruction mechanism is able to recover residual phase variations in speckled wavefronts emerging from volumetric scattering samples. a) and b) Scattered (speckled) phasemaps after the volumetric scattering sample with thickness $L = 720\mu m$ and scattering mean free path $\ell_s = 90\mu m$ for two different wavelengths $\lambda_1 = 690.00nm$ and $\lambda_2 = 690.23nm$. c) Calculated synthetic phase map for $\Lambda = 2.1mm$. d)-f) Same experiment with scatterer of different thickness ($L = 1080\mu m$) and optical wavelengths $\lambda_1 = 690.23nm$ and $\lambda_2 = 690.46nm$.

ceeding the SWL may be unambiguously recovered if the largest wavefront error Ψ_{max} introduced during light transport through the scattering scene fulfills a Rayleigh Quarter Wavelength criterion (RQWR [58]) for the SWL, i.e.,

$$\Psi_{max} \leq \frac{\Lambda}{4} \quad (2)$$

The wavefront error Ψ_{max} represents the worst-case spread in the physical lengths of scattered light paths that share a common source location, object location and detector pixel. For surface scattering processes, the spread in path lengths is limited by $2\sigma_h$, where σ_h represents the RMS surface roughness (see Eq. 40 in supplementary material). This is demonstrated experimentally in Fig. 4b-e. Using knowledge of the surface roughness of the 220 grit diffuser and the experimental geometry, we estimate Ψ_{max} to be $65\mu m$. Speckle artifacts are observed when Λ approaches $4\Psi_{max}$, consistent with the RQWR.

The supplementary material puts forth mathematical arguments supporting the existence of RQWR (Eq. 2) for a single realization of a scattering surface (see Section 1.6). The analysis shows how the RQWR fundamentally limits performance of a large class of NLoS imagers, including ToF techniques. Furthermore, the analysis may be generalized to include volumetric scatter by adopting a diffusive approach to light propagation [45]. It is observed that the spread in path lengths as determined by the ratio of the squared thickness of the medium L^2 to the transport mean free path ℓ^* , plays a role analogous to the RMS roughness σ_h of scattering surfaces.

The principal distinction between scattering at discrete interfaces such as walls and continuous scattering through a volume, lies in the scale of wavefront error Ψ_{max} . For instance, the typical wavefront error Ψ_{max} for 'imaging around corners' is less than 1 millimeter, several centimeters for imaging through tissue, and many meters for long-range imaging through fog. It is expected that diffusive scatter over long propagation distances will severely limit the maximal achievable resolution. In the specific case of imaging through fog, we anticipate that the time-gating ability of FMCW LiDAR [59] may be combined with SWH to see farther with a higher resolution than is otherwise possible. In the case of imaging through tissue, it is anticipated that ultrasound focusing aids may be combined with SWH to see farther into the brain with a higher resolution than is currently possible.

The notion of SWH as demonstrated in this paper has a broad range of applications including imaging through obscurants, fog, smoke, tissue, bone, face detection around corners, or 'pseudo-endoscopic' defect detection of mechanical assemblies during operation. These applications largely restrict attention to optical carrier frequencies. However, the true potential of our approach can be unlocked by transferring the notion to other wave phenomena. For instance, we envision the possibility of adapting the SWH principle to ultrasound imaging of biological features embedded deep within layers of tissue. Another example is coherent X-ray diffraction imaging of specimens embedded in thick, inhomogeneous samples. In both the examples, SWH has the potential to decouple the resolution of the reconstruction (de-

termined by the 'Synthetic Frequency') from the penetration depth (determined by the carrier frequency). We also envision the use of SWH in repurposing radio antenna arrays (e.g., the VLA) for space-based astronomical imaging at microwave and radio frequencies through dense atmosphere, and possibly below the surface of a planet for remote geological exploration. Using photonic mixers driven by continuous wave laser sources, it may be possible to simultaneously probe both optical reflectance and spectroscopic information of specimens by sensing THz synthetic wavelengths with optical detection techniques coupled together with direct sensing of THz electromagnetic signals. Moreover, we believe that the SWH concept has huge potential for Material Science, may it be to see deeper through materials or for the precise analysis of inhomogeneous or multi-layered structures.

There is much to be gained from exploiting spectral correlations in coherent light transport. Examining the SWH approach through the lens of Gabor holography provides newer insights into its operation and scope. Gabor originally conceived holography as a two-step process that involved recording an electron wave hologram and subsequently replaying it via optical diffraction. SWH can be interpreted as a generalization of Gabor's original analysis/synthesis technique, with an additional computation step. We hope that this novel view of SWH will help usher a diverse array of new research directions, in much the same manner as the invention of holography did decades ago.

432 Methods

433 **Formation of a synthetic wavelength hologram.** The 489
 434 wavefront aberration correction step adopted in SWH draws 490
 435 inspiration from multi-wavelength interferometry on rough 491
 436 surfaces [35–37]. The process illustrated in the right half 492
 437 of Fig. 2a involves recording speckle fields $E(\lambda_1), E(\lambda_2)$ 493
 438 at two closely spaced illumination wavelengths. Due to the 494
 439 stochastic nature of light scattering, the phase $\phi(\lambda_1), \phi(\lambda_2)$ 495
 440 of each field separately is completely randomized and bears 496
 441 no resemblance to the macroscopic structure of the object. If 497
 442 however, the illumination beams at the two wavelengths origi- 498
 443 nate from the same source position (such as from a single 499
 444 fiber) and the inhomogeneities in the scattering medium are 500
 445 quasi-static, then the fields incident on the detector are highly 501
 446 correlated. This is because the light at the two wavelengths 502
 447 *traverses nearly identical ray paths and experiences nearly* 503
 448 *identical path length fluctuations.* This assumption and obser- 504
 449 vation forms the basis of our computational approach to 505
 450 accommodating scattering where we correlate the complex- 506
 451 valued fields to recover the synthetic hologram $E(\Lambda) =$ 507
 452 $E(\lambda_1)E^*(\lambda_2)$, with $\Lambda = \frac{\lambda_1\lambda_2}{|\lambda_1 - \lambda_2|}$. It can be shown (see supple- 508
 453 mentary material) that the residual phase fluctuations in the 509
 454 synthetic hologram, given by $\phi(\Lambda) = \phi(\lambda_1) - \phi(\lambda_2)$, pre- 510
 455 serves phase variations at scales equal or larger than the SWL 511
 456 Λ , and is robust to speckle artifacts. However, the magnitude 512
 457 of the SWH, given by $|E(\Lambda)| = |E(\lambda_1)| \cdot |E(\lambda_2)|$, still ex- 513
 458 hibits speckle artifacts (see e.g. Fig. 2a). 514

459 **Interferometer design and lock-in detection of the syn-** 517
 460 **thetic hologram.** In practice, poor signal-to-background or 518
 461 signal-to-noise ratios, or both, can limit our ability to mea- 519
 462 sure objects at the smallest possible SWL that is defined by 520
 463 the RQWR (Eq. 2). Interferometric approaches exploiting 521
 464 *frequency heterodyning* have particularly advantageous prop- 522
 465 erties with respect to this problem. The principal benefit of 523
 466 adopting these approaches to record holograms is the ability 524
 467 to exploit the heterodyne gain [60] afforded by the use of a 525
 468 strong reference beam, whose baseband optical frequency is 526
 469 slightly detuned from the frequency of light in the object arm. 527
 470 The difference in frequency ν_m is chosen in the RF frequency 528
 471 range ($3kHz$ for our experiments) and realized by using a 529
 472 cascade of acousto-optic or electro-optic modulators (AOM 530
 473 or EOM). Figs. 4 a and b in the supplementary material de- 531
 474 pict the two interferometer designs that we use to acquire the 532
 475 holograms at the two optical wavelengths. Each design is an 533
 476 adaptation of a Michelson Interferometer, and incorporates a 534
 477 small difference ν_m in the baseband frequency of light in the 535
 478 two arms of the interferometer. It is emphasized that the RF 536
 479 modulation frequency ν_m is *fully decoupled* from the choice 537
 480 of SWL (and therefore from the resolution of our method!), 538
 481 and can be chosen independent of the SWL. 539

482 A Lock-In Focal Plane Array camera (LI-FPA) [61] capa- 529
 483 ble of synchronously demodulating the received irradiance 530
 484 at each detector pixel, is operated to detect the RF frequency 531
 485 ν_m . The process directly yields the interferogram at the 532
 486 SWL Λ . The method avoids the need for time consuming 533
 487 raster scanning as necessary in ToF-based techniques, and 534

488 phase-shifting of the optical signal. It also vastly improves 489
 489 the Signal-to-Background ratio of our measurements by 490
 490 suppressing the unmodulated ambient illumination. The 491
 491 Heliotis C3 LI-FPA [61] used in our experiments yields a 492
 492 300×300 *pix* image per measurement. The exposure time 493
 493 of each measurement is $t_{exp} = 23ms$ corresponding to 70 494
 494 cycles of the RF frequency $\nu_m = 3kHz$. Two independently 495
 495 tunable narrow linewidth CW lasers (Toptica DFB pro 496
 496 $855nm$) are used to illuminate and interrogate the scene. The 497
 497 center wavelength of each laser is $855nm$, and the maximum 498
 498 tuning range is $\sim 2.6nm$. This allows us to achieve SWLs 499
 499 $\Lambda \gtrsim 300\mu m$, corresponding to a beat frequencies $\lesssim 1THz$. 500

501 The holograms in our proof-of-principle experiments were 502
 502 recorded using two specific heterodyne interferometer archi- 503
 503 tectures: a Dual-Wavelength Heterodyne Interferometer 504
 504 (Fig. 4 a in the supplementary material), and a Superhetero- 505
 505 dyne Interferometer (Fig. 4 b in the supplementary material). 506
 506 The Dual-Wavelength Heterodyne Interferometer is preferred 507
 507 when light loss in the interferometer should be minimized, 508
 508 which is important for many NLoS applications. Light from 509
 509 the two lasers operating at λ_1, λ_2 are coupled together, be- 510
 510 fore being split into the reference and sample arm. The ref- 511
 511 erence arm is additionally modulated by $\nu_m = 3kHz$, using a 512
 512 cascade of two fiber AOM's. During acquisition, each laser 513
 513 is shuttered independently and the lock-in camera records 514
 514 the holograms at the two optical wavelengths, in a time- 515
 515 sequential manner. The LI-FPA provides two images: In- 516
 516 Phase (I) and Quadrature (Q), each of which represents the 517
 517 real and imaginary parts of the speckle fields incident on 518
 518 the image sensor. The expression for the I- and Q-images 519
 519 recorded by the LI-FPA for the wavelength λ_n is:

$$\begin{aligned} I_I(\lambda_n) &= A_n \cos(\phi(\lambda_n)) \\ I_Q(\lambda_n) &= A_n \sin(\phi(\lambda_n)) \end{aligned} \quad (3)$$

520 where A_n is the amplitude at λ_n and $\phi(\lambda_n)$ is the difference 521
 521 in the phase of light in the object and reference arms. Please 522
 522 note that Eq. 3 omits any reference to spatial locations, in 523
 523 the interest of clarity. Subsequently, the synthetic hologram 524
 524 $E(\Lambda)$ is assembled as follows:

$$\begin{aligned} E(\Lambda) &= [I_I(\lambda_1) + iI_Q(\lambda_1)] \cdot [I_I(\lambda_2) + i \cdot I_Q(\lambda_2)]^* \\ &= A_1 A_2 \exp(i(\underbrace{\phi(\lambda_1) - \phi(\lambda_2)}_{\phi(\Lambda)})) \end{aligned} \quad (4)$$

525 An attractive feature of the time-sequential approach to holo- 526
 526 gram acquisition described above is that it does not re- 527
 527 quire the use of two tunable lasers. Identical results can be 528
 528 achieved with one laser that is tuned between the two mea- 529
 529 surements. Possible extensions include: one tunable and one 530
 530 fixed wavelength laser, and one fixed wavelength laser that 531
 531 is split in two arms, one of which includes an additional fre- 532
 532 quency modulator.

533 Unfortunately, the simplicity of the time-sequential ap- 534
 534 proach comes at the expense of increased sensitivity to ob-

535 ject motion between measurements, and time-varying fluctu- 579
536 ations in the environmental conditions. Increased robustness 580
537 to these fluctuations is afforded by the Superheterodyne In- 581
538 terferometer design, wherein light from both lasers is used 582
539 to simultaneously illuminate the target and scene. A possible
540 realization is shown in Fig. 4b of the supplementary material:
541 each laser beam is split into two arms, where one of which is
542 independently modulated with an AOM. The RF drive fre-
543 quencies for AOMs 1A and 1B (see Fig. 4 b in the supple-
544 mentary material) are identically set to ν_{AOM1} , but include
545 a phase offset $\Delta\varphi_{AOM}$ that is user controlled. Light leaving
546 the two AOMs is combined and modulated with a third AOM
547 (frequency ν_{AOM2}), which produces the desired modulation 583
548 frequency $\nu_m = \nu_{AOM1} - \nu_{AOM2} = 3kHz$. The expression 584
549 for the I- and Q-images (In-Phase and Quadrature) recorded 585
550 by the LI-FPA after locking in at ν_m are:

$$\begin{aligned} I_I(\lambda_1, \lambda_2) &= A_1 \cos(\phi(\lambda_1) + \Delta\varphi_{AOM}) + A_2 \cos(\phi(\lambda_2)) \\ I_Q(\lambda_1, \lambda_2) &= A_1 \sin(\phi(\lambda_1) + \Delta\varphi_{AOM}) + A_2 \sin(\phi(\lambda_2)) \end{aligned} \quad (5)$$

551 The synthetic hologram $E(\Lambda)$ is assembled by calculating:

$$\begin{aligned} I_I^2 + I_Q^2 \\ = A_1^2 + A_2^2 + A_1 A_2 \underbrace{\cos(\phi(\lambda_1) - \phi(\lambda_2))}_{\phi(\Lambda)} + \Delta\varphi_{AOM} \end{aligned} \quad (6)$$

552 The synthetic phase map is eventually recovered from the 601
553 interferograms recorded with three or more phase shifts 602
554 $\Delta\varphi_{AOM}$ introduced between measurements. It should be 603
555 emphasized that the use of two tunable lasers is also not a pre- 604
556 requisite for this approach. Identical results can be achieved 605
557 with one fixed and one tuned laser, or similar combinations 606
558 discussed above. The principal benefit of the Superhetero- 607
559 dyne approach is the robustness to environmental fluctuations 608
560 and object motion. However, it requires an additional AOM 609
561 and fiber splitters that significantly reduce the available out- 610
562 put power compared to the Dual Wavelength Heterodyne In- 611
563 terferometer discussed previously. The loss of power presents 612
564 light throughput challenges for NLoS experiments that are in- 613
565 trinsically light starved. 614

566 In practice, there exists a trade-off between light through- 615
567 put and robustness to environmental fluctuations, which de- 616
568 pends on a multiple factors including stand-off distance, re- 617
569 flectivity of the involved surfaces, and laser power. 618

570 **Reference beam injection with reduced radiometric** 620
571 **losses.** The reference beam required for interferometric 621
572 sensing of the speckle fields at the optical wavelengths is di- 622
573 rected towards the lock-in FPA. In one possible embodiment, 623
574 a *lensed fiber needle* (WT&T Inc.) positioned in the front 624
575 focal plane of the imaging optic (see Fig. 4 f in the sup- 625
576plementary material) produces a near planar reference beam 626
577 on the FPA. The use of a lensed fiber provides two distinct 627
578 advantages over a beam-splitter: (1) the imaging optic can 628

be directly threaded to the camera (eliminates the need for
inserting beam splitter between optic and sensor) and easily
swapped during operation, and (2) improved light throughput
(see Tab. 1).

Light Loss in:	Reference Beam	Sample Beam
Lensed Fiber Needle	~ 30%	~ 0%
50/50 Beam Splitter	~ 50%	~ 50%

Table 1. Light loss at combination of reference and sample arm: Lensed fiber needle vs. conventional 50/50 beam splitter

Experimental setup and image formation for reflective NLoS imaging ('looking around corners'). The experimental apparatus schematically displayed in Fig. 2b, and shown in Fig. 4 c of the supplementary material is used to demonstrate the ability of SWH to discern objects obscured from view, in this case a cutout of the character 'N' with dimensions $\sim 20mm \times 15mm$. The size of the object was deliberately chosen to be smaller than the typical size of a resolution cell ($\sim 2cm$) in competing wide-field ToF-based approaches. The disadvantage when using a small object is that it emits less light than the background. The problem is additionally compounded by the limited laser power in the object arm (about $30mW$). In an effort to bypass these engineering limitations, we glued a thin sheet of silver foil to the sandblasted (280 grit) surface of the object 'N' and repeated the process for the VS surface. An image of object 'N' under ambient light can be seen in Fig. 3q. The fields reflected by these materials are fully developed speckle patterns. The VD wall surface is constructed from a standard dry-wall panel that has been painted white (Beer Eggshell paint).

Our approach to reflective NLoS imaging relies on the availability of an intermediary scattering surface (such as the wall in Fig. 2b) that serves to indirectly illuminate the obscured target and intercept the light scattered by the target. Accordingly, the intermediary surface may be viewed as a Virtualized Source (VS) of illumination and a Virtualized Detector (VD) for the obscured object.

Laser light from the physical source (at wavelengths λ_1 and λ_2) is directed towards the VS surface using a focusing optic. This light is scattered by the VS surface so as to illuminate the obscured object with a fully developed objective speckle pattern. A fraction of the light incident on the obscured object is redirected towards the VD surface. A second scattering event at the VD surface directs a tiny fraction of the object light towards the collection aperture, and subsequently the LI-FPA. The speckle fields impinging on the LI-FPA are synchronously demodulated to recover the real and imaginary parts of the holograms at the optical wavelengths λ_1 and λ_2 . Each of these holograms is additionally subject to diffraction due to the finite collection aperture. However, the diffraction effects are observed at optical wavelengths and have little impact on the SWL Λ . After assembling the synthetic hologram, the hidden object can be reconstructed by backpropagating the synthetic hologram, using a propagator (Free-Space propagator) at the SWL Λ . In the shown experiments, we used an angular spectrum propagator.

Figure 3 includes the result of processing the NLoS measurements acquired using the experimental setup of Fig. 2b. The measurements were captured at different SWLs ranging from $280\mu\text{m}$ to 2.6mm . Figure 3 shows five exemplary results for $\Lambda = 1.30\text{mm}$, $\Lambda = 920\mu\text{m}$, $\Lambda = 610\mu\text{m}$, $\Lambda = 560\mu\text{m}$ and $\Lambda = 440\mu\text{m}$. The phase of the synthetic hologram associated with each SWL is shown in Fig. 3 a-e. The phasemaps have been low-pass filtered with kernel size $\approx \Lambda$ for better visualization.

As discussed previously, the reconstruction resolution improves with decreasing SWL. However, decreasing the SWL leads to an increased spectral decorrelation of the speckle fields at the two optical wavelengths. The decorrelation manifests as excessive phase fluctuations in the SWH, which in turn produces increased speckle artifacts in the reconstructed images. The problem can be mitigated (to an extent) by exploiting speckle diversity at the VS, specifically by averaging over multiple speckle realizations of the virtualized illumination. In our experiment, we realized the speckle diversity by small movements of the VS position. The image insets in Figure 3f-j represent the result of incoherent averaging (intensity-averaging) of the backpropagated images, for 5 different VS positions. The improvement in reconstruction quality comes at the expense of increased number of measurements, but not unlike competing ToF-based approaches (e.g. $> 20,000$ VS positions are used in [17]). The distinction is that we need far fewer images. We conclude our discussion by observing that for static objects, the reconstruction quality may be further improved by increasing the number of VS positions used to realize speckle diversity.

Synthetic diffraction discs and lateral resolution. As seen in Figs. 3f-j, the resolution of the NLoS reconstruction improves with decreasing SWL Λ . This behavior is in complete agreement with results from classical holography. The diffraction limited resolution (minimum resolvable spot radius δx) of SWH can be quantified using Eq. 1, which succinctly captures the relationship between the SWL Λ and the highest resolution that can be achieved. A smaller SWL is clearly desirable since it leads to higher resolution *or* allows for a smaller VD surface (probing area) while keeping the resolution constant. We experimentally validate the above claim (and Eq. 1) by localizing a point-like source in the hidden volume, using a VD diameter of only $D = 58\text{mm}$. An exposed fiber connector positioned $z = 95\text{mm}$ behind the VD surface serves as a point-source. Holograms at the VD surface acquired with multiple optical wavelengths are processed to recover a multitude of synthetic holograms, each of which is digitally replayed to recover an image of the point-source. The experimentally observed spot sizes or 'synthetic diffraction discs', shown in Figs 3n-p, are consistent with theoretical predictions (red circles, calculated from Eq. 1), and increase with increasing SWL. For a SWL of $280\mu\text{m}$, we are able to achieve sub-millimeter resolution around the corner.

Experimental setup and image formation for transmissive NLoS imaging. The experimental apparatus schematically displayed in Fig. 2c is used to demonstrate the ability of SWH to image through scattering media. In a first experiment, we illuminate and image the character 'U' (see Fig. 3q) through an optically rough ground glass diffuser (220 grit). The geometry is unlike other transmission mode experiments wherein the object is illuminated directly [27] or sandwiched between two diffusers. The current choice of geometry is deliberate and designed to mimic the imaging of a target embedded in a scattering medium. Measurements were acquired for different SWLs ranging from $280\mu\text{m}$ to 2.6mm . Figures 4b-e show four exemplary reconstructions for $\Lambda = 1.30\text{mm}$, $\Lambda = 920\mu\text{m}$, $\Lambda = 360\mu\text{m}$, and $\Lambda = 280\mu\text{m}$. In each instance, we incoherently averaged the reconstruction results for two VS positions. A comparison of the image insets in Figures 4 confirms the increased decorrelation for decreasing SWL. As discussed previously, the wavefront error for the diffuser is estimated to be $\Psi \approx 65\mu\text{m}$, and the results for $\Lambda = 280\mu\text{m}$ demonstrate performance close to the limit expressed by Eq. 2.

In a second experiment the ground glass diffuser within the imaging path is swapped with a milky plastic plate of $\sim 4\text{mm}$ thickness. The plastic plate exhibits pronounced multiple scattering, representative of imaging through volumetric scatter. Figure 4a compares the visibility of a checkerboard viewed through the 220 grit ground glass diffuser and the plastic plate. In both cases, the checkerboard is positioned 1cm under the scattering plate and viewed under ambient illumination. It is evident from Figure 4a that the visibility of the checkerboard pattern is vastly diminished when viewed through the plastic plate, whereas the pattern is still visible when viewed through the diffuser.

Figure 4f-i shows reconstruction results for the same character 'U' as imaged through the plastic plate, for the same set of SWLs as the diffuser. In each instance, we incoherently averaged the reconstruction results for two VS positions. The character is reconstructed with high fidelity despite pronounced multiple scattering, suggesting the potential of SWH for imaging through volumetric scatter. A comparison of the image insets in Figures 4 confirms the diminished fidelity of imaging through volumetric scattering when compared to surface scatter.

ACKNOWLEDGEMENTS

This work was supported by DARPA through the DARPA REVEAL project (HR0011-16-C-0028), by NSF CAREER (IIS-1453192), and ONR (N00014-15-1-2735). The authors acknowledge the assistance of Mykola Kadobianskyi for making available the experimental data and supporting MATLAB scripts from [48]. The authors gratefully acknowledge the help of Zachary Lapin, Andreas Velten, Predrag Milojkovic, Gerd Häusler, Ravi Athale, and Joseph Mait in proofreading the manuscript and providing valuable comments.

Bibliography

- [1] Isaac Freund. Looking through walls and around corners. *Physica A: Statistical Mechanics and its Applications*, 168(1):49 – 65, 1990. ISSN 0378-4371. doi: [https://doi.org/10.1016/0378-4371\(90\)90357-X](https://doi.org/10.1016/0378-4371(90)90357-X).
- [2] L. WANG, P. P. HO, C. LIU, G. ZHANG, and R. R. ALFANO. Ballistic 2-d imaging through scattering walls using an ultrafast optical kerr gate. *Science*, 253(5021):769–771, 1991. ISSN 0036-8075. doi: 10.1126/science.253.5021.769.

- 741 [3] Seokchan Yoon, Moonseok Kim, Mooseok Jang, Youngwoon Choi, Wonjun Choi, Sungsam 827
742 Kang, and Wonshik Choi. Deep optical imaging within complex scattering media. *Nature* 828
743 *Reviews Physics*, 2(3):141–158, February 2020. doi: 10.1038/s42254-019-0143-2. 829
- 744 [4] Vasilis Ntziachristos. Going deeper than microscopy: the optical imaging frontier in biology. 830
745 *Nature Methods*, 7, 2010. 831
- 746 [5] C. Dunsby and P.M.W. French. Techniques for depth-resolved imaging through turbid media 832
747 including coherence-gated imaging. *J. Phys. D: Appl. Phys.* 36, 2003. 833
- 748 [6] Yoko Hoshi M.D. and Yukio Yamada. Overview of diffuse optical tomography and its clinical 834
749 applications. *Journal of Biomedical Optics*, 21(9):1 – 11, 2016. doi: 10.1117/1.JBO.21.9. 835
750 091312. 836
- 751 [7] K. M. Yoo and R. R. Alfano. Time-resolved coherent and incoherent components of forward 837
752 light scattering in random media. *Opt. Lett.*, 15(6):320–322, Mar . 838
- 753 [8] Jacopo Bertolotti, Elbert Putten, Christian Blum, Ad Lagendijk, Willem Vos, and Allard Mosk. 839
754 Non-invasive imaging through opaque scattering layers. *Nature*, 491:232–4, 11 2012. doi: 840
755 10.1038/nature11578. 841
- 756 [9] Allard Mosk, Ad Lagendijk, Geoffroy Lerosey, and Mathias Fink. Controlling waves in space 842
757 and time for imaging and focusing in complex media. *Nature Photonics*, 6:283–292, 05 843
758 2012. doi: 10.1038/nphoton.2012.88. 844
- 759 [10] Zahid Yaqoob, Demetri Psaltis, Michael Feld, and Changhui Yang. Optical phase conjuga- 845
760 tion for turbidity suppression in biological samples. *Nature photonics*, 2:110–115, 02 2008. 846
761 doi: 10.1038/nphoton.2007.297. 847
- 762 [11] Ivo Micha Vellekoop, Aart Lagendijk, and Allard Mosk. Exploiting disorder for perfect focus- 848
763 ing. *Nature photonics*, 4:320–322, 2010. ISSN 1749-4885. doi: 10.1038/nphoton.2010.3. 849
764 doi:10.1038/nphoton.2010.3. 850
- 765 [12] Xiao Xu, Honglin Liu, and Lihong Wang. Time-reversed ultrasonically encoded optical focus- 851
766 ing into scattering media. *Nature photonics*, 5:154, 03 2011. doi: 10.1038/nphoton.2010.306. 852
- 767 [13] Daniel Doktotsky, Moriya Rosenfeld, and Ori Katz. Acousto optic imaging beyond the acous- 853
768 tic diffraction limit using speckle decorrelation. *Communications Physics*, 3:5, 12 2020. doi: 854
769 10.1038/s42005-019-0267-9. 855
- 770 [14] Daniele Faccio, Andreas Velten, and Gordon Wetzstein. Non-line-of-sight imaging. *Nature* 856
771 *Reviews Physics*, 2:318–327, 2020. 857
- 772 [15] M. Batarseh, S. Sukov, Z. Shen, H Gemar, R. Rezvani, and A. Dogariu. Passive sensing 858
773 around the corner using spatial coherence. *Nature Communications* 9, 3629 (2018). 859
- 774 [16] Matthew O’Toole, David Lindell, and Gordon Wetzstein. Confocal non-line-of-sight imaging 860
775 based on the light-cone transform, *Nature* (2018). 861
- 776 [17] Xiaochun Liu, Ibon Guillen, Marco La Manna, Ji Hyun Nam, Syed Azer Reza, Toan Huu 862
777 Le, Adrian Jarabo, Diego Gutierrez, and Andreas Velten. Non-line-of-sight imaging using 863
778 phasor-field virtual wave optics. *Nature* (2019). 864
- 779 [18] Andreas Velten, Thomas Willwacher, Otkrist Gupta, Ashok Veeraraghavan, Mounsi 865
780 Bawendi, and Ramesh Raskar. Recovering three-dimensional shape around a corner using 866
781 ultrafast time-of-flight imaging. *Nature Communications* (2012). 867
- 782 [19] Daniele Faccio. Non-line-of-sight imaging. *Opt. Photon. News*, 30(1):36–43, Jan 2019. 868
- 783 [20] Ori Katz, Pierre Heidmann, Mathias Fink, and Sylvain Gigan. Non-invasive single-shot imag- 869
784 ing through scattering layers and around corners via speckle correlations. *Nature photonics*, 870
785 8(10):784, 2014. 871
- 786 [21] Ori Katz, Eran Small, and Yaron Silberberg. Looking around corners and through thin turbid 872
787 layers in real time with scattered incoherent light. *Nature Photonics*, 6:549–553, 2012. 873
- 788 [22] David B Lindell and Gordon Wetzstein. Three-dimensional imaging through scattering me- 874
789 dia based on confocal diffuse tomography. *Nature Communications*, 11(1):1–8, 2020. 875
- 790 [23] Genevieve Gariepy, Francesco Tonolini, Robert Henderson, Jonathan Leach, and Daniele 876
791 Faccio. Detection and tracking of moving objects hidden from view. *Nature photonics*, 10, 877
792 2016. 878
- 793 [24] Florian Willomitzer, Fengqiang Li, Muralidhar Madabhushi Balaji, Prasanna Rangarajan, 879
794 and Oliver Cossairt. High resolution non-line-of-sight imaging with superheterodyne remote 880
795 digital holography. In *Imaging and Applied Optics 2019 (COSI, IS, MATH, pcAOP)*, page 881
796 CM2A.2. Optical Society of America, 2019. doi: 10.1364/COSI.2019.CM2A.2. 882
- 797 [25] Prasanna Rangarajan, Florian Willomitzer, Oliver Cossairt, and Marc P. Christensen. Spa- 883
798 tially resolved indirect imaging of objects beyond the line of sight. In Jean J. Dolne, Mark F. 884
799 Spencer, and Markus E. Testorf, editors, *Unconventional and Indirect Imaging, Image Re- 885*
800 *construction, and Wavefront Sensing 2019*, volume 11135, pages 124 – 131. International 886
801 Society for Optics and Photonics, SPIE, 2019. doi: 10.1117/12.2529001. 887
- 802 [26] Eitan Dreier and Giuliano Scarcelli. Optical imaging through dynamic turbid media using the 888
803 fourier-domain shower-curtain effect. *Optica*, 3(1):71–74, Jan 2016. doi: 10.1364/OPTICA. 889
804 3.000071. 890
- 805 [27] Alok Kumar Singh, Dinesh N. Naik, Giancarlo Pedrini, Mitsuo Takeda, and Wolfgang Osten. 891
806 Looking through a diffuser and around an opaque surface: A holographic approach. *Opt.* 892
807 *Express*, 22(7):7694–7701, Apr 2014. doi: 10.1364/OE.22.007694. 893
- 808 [28] Aparna Viswanath, Prasanna Rangarajan, Duncan MacFarlane, and Marc P. Christensen. 894
809 Indirect imaging using correlography. In *Imaging and Applied Optics 2018 (3D, AO, AIO, 895*
810 *COSI, DH, IS, LACSEA, LS&C, MATH, pcAOP)*, page CM2E.3. Optical Society of America, 896
811 2018. doi: 10.1364/COSI.2018.CM2E.3. 897
- 812 [29] Muralidhar Madabhushi Balaji, Prasanna Rangarajan, Duncan MacFarlane, Andreas Cor- 898
813 liano, and Marc P. Christensen. Single-shot holography using scattering surfaces. In *Imag- 899*
814 *ing and Applied Optics 2017 (3D, AIO, COSI, IS, MATH, pcAOP)*, page CTu2B.1. Optical 900
815 Society of America, 2017. doi: 10.1364/COSI.2017.CTu2B.1. 901
- 816 [30] Isaac Freund, M. Rosenbluh, and Shechao Feng. Memory effects in propagation of optical 902
817 waves through disordered media. *Physical review letters*, 61:2328–2331, 12 1988. doi: 903
818 10.1103/PhysRevLett.61.2328. 904
- 819 [31] JW. Goodman. Speckle phenomena in optics: theory and applications , Roberts and Com- 905
820 pany Publishers; 2007. 906
- 821 [32] Sébastien Popoff, Geoffroy Lerosey, R Carminati, Mathias Fink, and S Gigan. Measuring the 907
822 transmission matrix in optics: An approach to the study and control of light propagation in 908
823 disordered media. *Physical review letters*, 104:100601, 03 2010. doi: 10.1103/PhysRevLett. 909
824 104.100601. 910
- 825 [33] Sébastien Popoff, Geoffroy Lerosey, Mathias Fink, Claude Boccara, and Sylvain Gigan. 911
826 Image transmission through an opaque material. *Nature communications*, 1:81, 09 2010. 912
- doi: 10.1038/ncomms1078. 913
- [34] Paul Sava and Erik Asphaug. Seismology on small planetary bodies by orbital laser doppler 914
vibrometry. *Advances in Space Research*, 64(2):527 – 544, 2019. ISSN 0273-1177. doi: 915
https://doi.org/10.1016/j.asr.2019.04.017. 916
- [35] A. F. Fercher, H. Z. Hu, and U. Vry. Rough surface interferometry with a two-wavelength 917
heterodyne speckle interferometer. *Appl. Opt.*, 24(14):2181–2188, Jul 1985. doi: 10.1364/ 918
AO.24.002181. 919
- [36] U. Vry and A. F. Fercher. Higher-order statistical properties of speckle fields and their ap- 920
plication to rough-surface interferometry. *J. Opt. Soc. Am. A*, 3(7):988–1000, Jul 1986. doi: 921
10.1364/JOSAA.3.000988. 922
- [37] R. Dändliker, R. Thalmann, and D. Prongué. Two-wavelength laser interferometry using 923
superheterodyne detection. *Opt. Lett.*, 13(5):339–341, May 1988. doi: 10.1364/OL.13. 924
000339. 925
- [38] Bernd Ruffing and Jürgen Fleischer. Spectral correlation of partially or fully developed 926
speckle patterns generated by rough surfaces. *J. Opt. Soc. Am. A*, 2(10):1637–1643, Oct 927
1985. doi: 10.1364/JOSAA.2.001637. 928
- [39] Aniceto Belmonte. Statistical model for fading return signals in coherent lidars. *Appl. Opt.*, 929
49(35):6737–6748, Dec 2010. doi: 10.1364/AO.49.006737. 930
- [40] B. Shapiro. Large intensity fluctuations for wave propagation in random media. *Phys. Rev.* 931
Lett., 57:2168–2171, Oct 1986. doi: 10.1103/PhysRevLett.57.2168. 932
- [41] A.Z. Genack and J. M. Drake. Relationship between optical intensity, fluctuations and pulse 933
propagation in random media., *EPL (Europhysics Letters)* 11.4 (1990): 331. 934
- [42] Johannes F. de Boer, Meint P. van Albada, and Ad Lagendijk. Transmission and intensity 935
correlations in wave propagation through random media. *Phys. Rev. B*, 45:658–666, Jan 936
1992. doi: 10.1103/PhysRevB.45.658. 937
- [43] Eric Akkermans and Gilles Montambaux. *Mesoscopic Physics of Electrons and Photons.* 938
Cambridge University Press, 2007. doi: 10.1017/CBO9780511618833. 939
- [44] Alesya Mikhailovskaya, Julien Fade, and Jerome Crassous. Speckle decorrelation with 940
wavelength shift as a simple way to image transport mean free path, *The European Physical* 941
Journal Applied Physics 85.3 (2019): 30701. 942
- [45] Charles A. Thompson, Kevin J. Webb, and Andrew M. Weiner. Diffusive media character- 943
ization with laser speckle. *Appl. Opt.*, 36(16):3726–3734, Jun 1997. doi: 10.1364/AO.36. 944
003726. 945
- [46] MP Van Albada, JF De Boer, and A Lagendijk. Observation of long-range intensity correla- 946
tion in the transport of coherent light through a random medium. *Physical review letters*, 64 947
(23):2787, 1990. 948
- [47] Beer. Bestimmung der absorption des rothen lichts in farbigen flüssigkeiten. *Annalen der* 949
Physik, 162(5):78–88, 1852. doi: 10.1002/andp.18521620505. 950
- [48] Mykola Kadobianskyi, Ioannis N Papadopoulos, Thomas Chaigne, Roarke Horstmeyer, and 951
Benjamin Judkewitz. Scattering correlations of time-gated light. *Optica*, 5(4):389–394, 2018. 952
- [49] Maciej Wojtkowski. High-speed optical coherence tomography: basics and applications. 953
Appl. Opt., 49(16):D30–D61, Jun 2010. doi: 10.1364/AO.49.000D30. 954
- [50] Peter Andretzky, Michael W. Lindner, Juergen M. Herrmann, A. Schultz, M. Konzog, 955
F. Kieseewetter, and Gerd Haeusler. Optical coherence tomography by spectral radar: dy- 956
namic wave estimation and in-vivo measurements of skin. In Marco Dal Fante, Hans- 957
Jochen Foth, Neville Krasner M.D., Renato Marchesini, and Halina Podbielska M.D., edi- 958
tors, *Optical and Imaging Techniques for Biomedicine IV*, volume 3567, pages 78 – 87. 959
International Society for Optics and Photonics, SPIE, 1999. doi: 10.1117/12.339173. 960
- [51] A F Fercher and E Roth. Ophthalmic Laser Interferometry. In Gerhard J. Mueller, editor, 961
Optical Instrumentation for Biomedical Laser Applications, volume 0658, pages 48 – 51. 962
International Society for Optics and Photonics, SPIE, 1986. doi: 10.1117/12.938523. 963
- [52] D Huang, EA Swanson, CP Lin, JS Schuman, WG Stinson, W Chang, MR Hee, T Flotte, 964
K Gregory, CA Puliiafito, and al. et. Optical coherence tomography. *Science*, 254(5035): 965
1178–1181, 1991. ISSN 0036-8075. doi: 10.1126/science.1957169. 966
- [53] E. N. Leith and G. J. Swanson. Achromatic interferometers for white light optical processing 967
and holography. *Appl. Opt.*, 19(4):638–644, Feb 1980. doi: 10.1364/AO.19.000638. 968
- [54] Thomas Dresel, Gerd Häusler, and Holger Venzke. Three-dimensional sensing of rough 969
surfaces by coherence radar. *Appl. Opt.*, 31(7):919–925, Mar 1992. doi: 10.1364/AO.31. 970
000919. 971
- [55] Jun Ye. Absolute measurement of a long, arbitrary distance to less than an optical fringe. 972
Opt. Lett., 29(10):1153–1155, May 2004. doi: 10.1364/OL.29.001153. 973
- [56] Seung-Woo Kim. Metrology: combs rule, *Nature photonics* 3.6 (2009): 313. 974
- [57] Jonghan Jin. Dimensional metrology using the optical comb of a mode-locked laser, *Mea- 975*
surement Science and Technology 27.2 (2015): 022001. 976
- [58] Lord Rayleigh, *Philos. Mag.* 8, 403 (1879). Reprinted in his *Scientific Papers* (Cambridge U. 977
Press, 1899), Vol. 1, pp. 432-435. 978
- [59] Jesse Zheng. *Optical frequency-modulated continuous-wave (FMCW) interferometry*, vol- 979
ume 107. Springer Science & Business Media, 2005. 980
- [60] Yan Liu, Cheng Ma, Yuecheng Shen, and Lihong V. Wang. Bit-efficient, sub-millisecond 981
wavefront measurement using a lock-in camera for time-reversal based optical focusing 982
inside scattering media. *Opt. Lett.*, 41(7):1321–1324, Apr 2016. doi: 10.1364/OL.41.001321. 983
- [61] Heliotis. Helicam C3 , https://www.heliotis.ch/html/lockInCameraC3.htm). 984